








Triggering superconductivity, semiconducting states, and ternary valley structure in graphene via functionalization with Si-N layers

Luo Yan ^{1,*}, Jiaojiao Zhu ^{2,*}, Bao-Tian Wang ³, Peng-Fei Liu ³, Guangzhao Wang ⁴,
Shengyuan A. Yang ^{2,†} and Liujiang Zhou ^{1,5,‡}

¹*School of Physics, University of Electronic Science and Technology of China, Chengdu 610054, China*

²*Research Laboratory for Quantum Materials, Singapore University of Technology and Design, Singapore 487372, Singapore*

³*Institute of High Energy Physics, Chinese Academy of Science (CAS), Beijing 100049, China*

⁴*School of Electronic Information Engineering, Yangtze Normal University, Chongqing 408100, China*

⁵*Yangtze Delta Region Institute (Huzhou), University of Electronic Science and Technology of China, Huzhou 313001, China*



(Received 11 September 2022; revised 27 January 2023; accepted 30 January 2023; published 14 February 2023)

Opening a band gap and realizing static valley control have been long sought in graphene-based two-dimensional (2D) materials. Motivated by the recent success in synthesizing 2D materials passivated by Si-N layers, here, we propose two new graphene-based materials, 2D C₂SiN and CSiN, via first-principles calculations. Monolayer C₂SiN is metallic and realizes superconductivity at low temperatures. Monolayer CSiN enjoys excellent stability and a mechanical property. It is a semiconductor with a ternary valley structure for electron carriers. Distinct from existing valleytronic platforms, these valleys can be controlled by applied uniaxial strain. The valley polarization of carriers further manifests as a pronounced change in the anisotropic conductivity, which can be detected in simple electric measurement. The strong interaction effects also lead to large exciton binding energy and enhance the optical absorption in the ultraviolet range. Our paper opens a new route to achieve superconductivity, ternary valley structure, and a semiconductor with enhanced optical absorption in 2D materials.

DOI: [10.1103/PhysRevB.107.085413](https://doi.org/10.1103/PhysRevB.107.085413)

I. INTRODUCTION

Graphene has attracted tremendous research interest in the past 20 years, owing to its excellent electric, mechanical, and optical properties [1,2]. The study of graphene also boosted the development of the field of valleytronics [3]. In graphene, the low-energy carriers are located at two energy degenerate valleys in the momentum space, and it was proposed that this binary valley degree of freedom can be used to encode and process information, analogous to the idea in spintronics [4–6].

In pushing graphene towards electronic applications, a big challenge comes from the absence of a band gap in graphene. There is a tiny gap opened by spin-orbit coupling (SOC) [7,8], which can be safely neglected for most purposes. Pristine graphene is a semimetal where the π bands, derived from the $C-p_z$ orbitals, cross at two inequivalent Dirac points on the Fermi level, forming the two-valley structure [2]. Many schemes for opening a band gap in graphene have been proposed. One most direct approach is surface functionalization, i.e., to use the adsorbed atoms or functional groups to saturate the low-energy p_z orbitals. For example, the hydrogenated or fluorinated graphene two-dimensional (2D) structures were extensively studied and some successfully demonstrated in ex-

periment as good semiconductors [9,10]. Nevertheless, these resulting structures often lack good thermal/mechanical stability and their carrier mobility is often severely degraded. Moreover, the valley structure of graphene is usually destroyed in the functionalization process.

Very recently, centimeter-scale monolayers (MLs) of the MoSi₂N₄ family materials have been successfully synthesized via a novel chemical vapor deposition growth method [11]. The structure of MoSi₂N₄ can be viewed as a MoN₂ ML passivated by Si-N layers on its two sides. ML MoN₂ is metallic; after the Si-N functionalization, the resulting MoSi₂N₄ becomes a semiconductor with a band gap of ~ 1.94 eV. The similar phase transitions also appear for metallic WN₂ and CrN₂ MLs when functionalized by Si-N layers [11,12]. In addition, the Si-N layers can significantly improve the mechanical and thermodynamic stabilities of these 2D materials, and in some cases it leads to interesting physics, such as valley-spin coupling, nontrivial band topology, 2D superconductivity, and piezoelectricity [13–15].

Motivated by the above-mentioned experimental and theoretical progress, in this paper, using first-principles calculations, we explore the 2D structures formed by graphene passivated with Si-N layers. Specifically, we consider ML C₂SiN and CSiN. The former has a Si-N layer attached on only one side of graphene, whereas the latter has Si-N layers on both sides. We show that C₂SiN is a 2D metal and exhibits superconductivity with an estimated $T_c \sim 1.01$ K. On the other hand, the 2D CSiN has excellent stability and mechanical property. It is a good semiconductor with band gap > 3 eV.

*These authors contributed equally to this work.

†shengyuan_yang@sutd.edu.sg

‡liujiang86@gmail.com

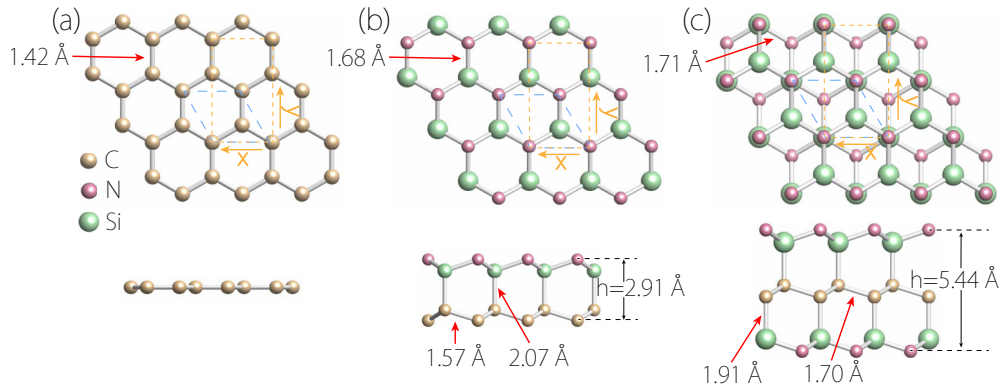


FIG. 1. Top (upper panel) and side (lower panel) views for (a) pristine graphene, (b) ML C_2SiN , and (c) ML $CSiN$. The blue dashed lines mark the primitive cell, and the orange dashed lines indicate the rectangular conventional cell.

We find that ML $CSiN$ can maintain a high electron carrier mobility $\sim 2000 \text{ cm}^2 \text{ V}^{-1} \text{ S}^{-1}$. Remarkably, 2D $CSiN$ possesses a novel ternary valley structure at the conduction-band edge. The three valleys are connected by the C_{3z} symmetry, so the valley splitting and valley polarization in 2D $CSiN$ can be readily controlled by applying an uniaxial strain, which singles out a particular valley label. This is in contrast to the graphene or transition-metal dichalcogenides materials where the valleys are connected by time-reversal symmetry and the strain control of valley splitting is forbidden. We show that for ML $CSiN$, a very large valley splitting $>0.6 \text{ eV}$ can be generated at a moderate strain $\sim 5\%$. Importantly, the valley polarization can result in a highly anisotropic electron transport character. In addition, we predict strong excitonic effects in ML $CSiN$ with large exciton binding energy $\sim 1 \text{ eV}$ and strong absorption peak $\sim 5 \text{ eV}$. Our paper provides a new strategy towards graphene-based 2D materials and reveals a new 2D semiconductor platform with novel valleytronic functionalities and excellent mechanical, electronic, and optical performances.

II. COMPUTATIONAL METHODS

Our first-principles calculations are based on the density functional theory, performed using the Perdew-Burke-Ernzerhof (PBE) functional for the exchange-correlation potential [16,17] as implemented in the Vienna *ab initio* simulation package (VASP) [18,19]. The projector augmented-wave method was adopted to simulate the ionic potentials [16]. The optB88-vdW approach was used to model the van der Waals interactions [20]. SOC is very weak in the studied materials since they only involve light elements, and we have tested that SOC has little effect on the band structure. Hence, the results presented in the paper are without SOC. The kinetic-energy cutoff of 450 eV and the k -point mesh of $25 \times 25 \times 1$ were employed in the calculations. To avoid the artificial interactions between periodic images, a vacuum space of 15 Å was inserted along the z direction. The phonon properties were studied within the density functional perturbation theory with the PHONOPY code [21]. The *ab initio* molecular dynamics (AIMD) simulations with the Nosé-Hoover thermostat [22] were used to evaluate the thermal stability and a $4 \times 4 \times 1$ supercell was taken for the simulation. Some data postpro-

cessing after VASP calculations was performed by using the VASPKIT code [23]. The QUANTUM ESPRESSO (QE) package [24,25] was used to study the superconductivity within the Bardeen-Cooper-Schrieffer (BCS) theory [26–28]. Detailed methods for calculating superconductivity were available in the Supplemental Material [29] (see also Refs. [26–28,30] therein). To study the excitonic effect, based on the ground-state Kohn-Sham energies and wave functions obtained from QE self-consistent calculations, YAMBO software [31] was adopted to model the screened Coulomb interactions (G_0W_0 approximation) in combination with the random phase approximation (RPA) or the Bethe-Salpeter equation (BSE). In order to converge the quasiparticle energy gap, the total number of bands were set to be ten times the valence bands, and the cutoff energy was set to be 8 Ry for the response function in the G_0W_0 step. The five highest valence bands and five lowest conduction bands were taken to describe the excitons in the BSE calculation.

III. RESULTS AND DISCUSSION

A. Crystal structures of ML C_2SiN and $CSiN$

The crystal structures of ML C_2SiN and $CSiN$ are illustrated in Figs. 1(b) and 1(c). They are constructed by attaching Si-N layers to the ML graphene, similar to the formation of $MoSi_2N_4$ [11]. The two crystals share the same space group of $P3m1$ (No. 156) with the C_{3v} point group, which is distinct from the D_{6h} point-group symmetry for ML graphene [see Fig. 1(a)]. The optimized lattice parameters for ML C_2SiN and $CSiN$ are 2.70 and 2.81 Å, respectively. In ML C_2SiN , the C-C, C-Si, and Si-N bond lengths are found to be 1.57, 2.07, and 1.68 Å, respectively. In ML $CSiN$, the C-C and Si-N bond lengths are elongated to 1.70 and 1.71 Å, respectively, whereas the C-Si bond length decreases to 1.91 Å. Notably, in both materials, the graphene layer becomes puckered. The puckering height is about 0.2 Å in ML C_2SiN and 0.5 Å in ML $CSiN$. The detailed structural data for the two materials are provided in Supplemental Material Tables S1 and S2 [29].

To investigate the bonding character, the electron localization function (ELF) is evaluated (see the Supplemental Material Fig. S1 [29]). The result shows that all bonds in the two structures are strong covalent type. Particularly, by forming the Si-C bonds, the Si atoms saturate the C-

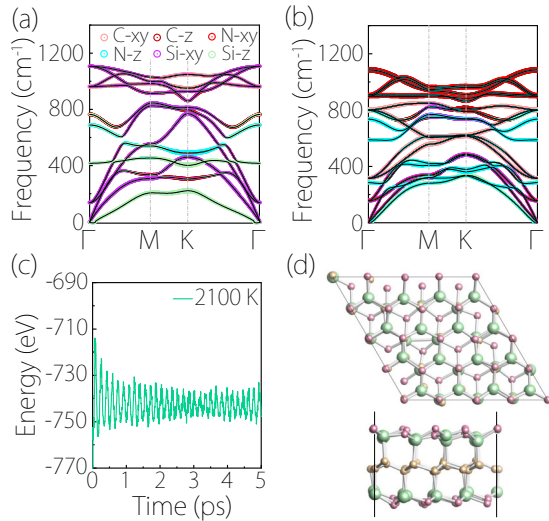


FIG. 2. Phonon spectra of (a) ML C_2SiN and (b) ML $CSiN$. The colored weight indicates projection onto vibrational modes of Si, C, and N atoms. (c) Energy variation of ML $CSiN$ during the AIMD simulation at 2100 K. (d) shows the last snapshots from the top and side views.

p_z orbitals underneath them. The puckered structure of the graphene layer also indicates an evolution from sp^2 to sp^3 orbital hybridization for the C atoms.

B. Stability and mechanical property

The dynamic stabilities of the two materials can be inferred from their phonon spectra, as plotted in Figs. 2(a) and 2(b). The absence of imaginary frequencies in the spectra verifies their dynamic stabilities. One notes that the highest phonon frequency can reach $\sim 1100 \text{ cm}^{-1}$, which is comparable to that of borophene ($\sim 1200 \text{ cm}^{-1}$) [32], manifesting their strong bonding interactions among the component atoms [33,34]. In the vicinity of the Γ point, the out-of-plane transverse acoustic (ZA) mode and the in-plane transverse (TA) and longitudinal acoustic (LA) modes can be visualized. Analysis of the vibration modes shows that the ZA mode mostly involves the out-of-plane vibration of the Si atoms, whereas the LA and TA modes are related mainly to the in-plane vibration of Si atoms. We observe that the obtained ZA dispersion is not perfectly quadratic. This should be an artifact due to numerical errors in calculating the interatomic force constants that slightly break rotation/translation symmetries [35].

We subsequently evaluate the thermal stability of the two materials by performing AIMD simulations. We find that ML C_2SiN can maintain its structural integrity only around 100 K (see the Supplemental Material Fig. S2 [29]). In contrast, ML $CSiN$ is much more stable. Its average value of the energy remains nearly constant with small fluctuations during the entire simulation and no obvious bond breakage at temperature up to 2100 K [see Figs. 2(c) and 2(d)], showing an extremely high melting point.

Next, we investigate the mechanical properties of ML C_2SiN and $CSiN$. For this kind of calculation, it is more convenient to take a rectangle unit cell as shown in Fig. 1. The results show that the linear elastic regimes for ML C_2SiN and

$CSiN$ can be up to 5% strain (see the Supplemental Material Fig. S3 [29]). Beyond this regime, the plastic deformation arises. The critical strain (i.e., the maximal strain the material can sustain) for the two materials can reach a high value $\sim 20\%$ for both biaxial strain and uniaxial strain along the y direction. The critical uniaxial strain along the x direction is smaller. It is $\sim 13\%$ and 9% for ML C_2SiN and $CSiN$, respectively. These results are also supported by their strain-energy curves (see the Supplemental Material Fig. S3 [29]). The elastic properties of each structure can be characterized by four independent elastic constants: C_{11} , C_{12} , C_{22} , and C_{66} , which have been evaluated in our calculations. We confirm that they satisfy the Born criterion for the rectangular cell [36], namely, $C_{11} > 0$, $C_{66} > 0$, and $C_{11} \times C_{22} > C_{12}^2$, indicating that the two materials are mechanically stable. Due to the ambiguity in defining the thickness of a 2D structure, we employ the 2D Young's modulus Y^{2D} to quantify the in-plane stiffness [37,38]. This value is obtained by the relation $Y_x^{2D} = (C_{11}^2 - C_{12}^2)/C_{22}$ and $Y_y^{2D} = (C_{11}^2 - C_{12}^2)/C_{11}$. Using this method, the calculated in-plane stiffness for graphene is 333 N/m , which agrees well with the experimental value of $340 \pm 50 \text{ N/m}$ [39]. The in-plane stiffness values for ML C_2SiN and $CSiN$ are calculated to be 382 and 427 N/m , respectively. These values are larger than graphene (340 N/m) [39], hexagonal boron nitride (258 N/m) [40], and MoS_2 (140 N/m) [41], reflecting their strong bonding characters. In addition, the Poisson's ratio (ν) can be obtained from $\nu_x = C_{12}/C_{22}$ and $\nu_y = C_{12}/C_{11}$. We find that $\nu_x \approx \nu_y = 0.19$ and 0.26 for ML C_2SiN and $CSiN$, respectively. More detailed results are given in the Supplemental Material Table S3 [29].

C. Metallicity and superconductivity in ML C_2SiN

The orbital projected band structure of ML C_2SiN is presented in Fig. 3(b). For comparison, we also plot the band structure of graphene in Fig. 3(a). One observes that ML C_2SiN is metallic with a single quite flat band crossing the Fermi level. This can be readily understood as following. As discussed, in graphene, the low-energy states are derived from the $C-p_z$ orbitals. In ML C_2SiN , half of the C atoms in the graphene layer are bonded with the Si atoms in the Si-N layer with their corresponding p_z orbitals passivated. Nevertheless, there are still other half C atoms unpassivated. Their p_z orbitals remain at the Fermi level, and the bandwidth is decreased due to the suppressed hopping amplitude. Indeed, the orbital projection in Fig. 3(b) clearly shows that this band is dominated by the p_z orbitals of the unpassivated C atoms, confirming our expectation.

It is known that the pristine graphene is not a superconductor due to its small density of states around the Fermi level and its very weak electron-phonon coupling strength [2,42]. Interestingly, we find that ML C_2SiN can exhibit BCS-type superconductivity. We compute the branch magnitude of the electron-phonon coupling (EPC) λ_{qv} as shown in Fig. 4, which determines the contribution to EPC constant λ from the individual phonon branch. One can see that the main contribution originates from the low-frequency region (below 450 cm^{-1}). In this region, the Eliashberg spectral function $\alpha^2F(\omega)$ shows two significant peaks, at 200 and 430 cm^{-1} , leading to a rapid increase in the cumulative $\lambda(\omega)$, about 75%

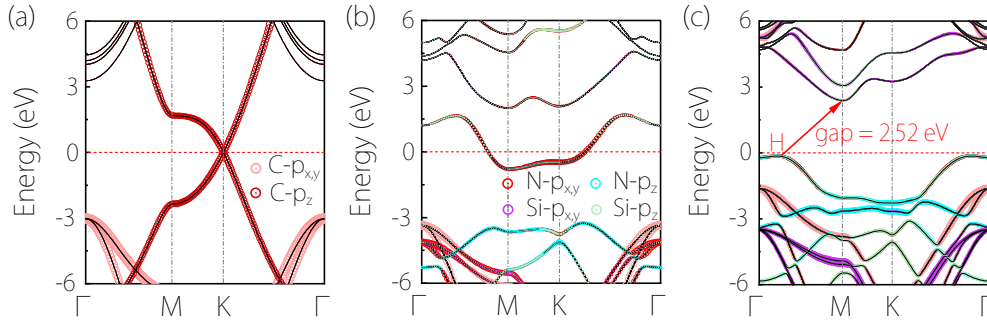


FIG. 3. Band structures of (a) graphene, (b) ML C_2SiN , and (c) ML $CSiN$ obtained from first-principles calculations. Projection weights of the band states onto different atomic orbitals are indicated.

of the total EPC ($\lambda = 0.32$). Physically, the main coupling is between the C - p_z orbitals and the out-of-plane vibration modes. Based on the simplified McMillian-Allen-Dynes formula [30], we estimate that the T_c of ML C_2SiN is ~ 1.01 K, which is not high but comparable to the magic-angle-twisted bilayer graphene (1.70 K) [42]. In addition, biaxial strain can further enhance the T_c (to ~ 7 K at the 10% strain) as shown in the Supplemental Material Fig. S4 [29]. Our result demonstrates that superconductivity can be introduced into graphene through surface functionalizations, which opens a new route for achieving superconductivity in 2D graphene-based materials.

D. Ternary valley structure and valley control in ML $CSiN$

Now we turn to ML $CSiN$, which is structurally more robust. Since all the C atoms are bonded with Si atoms in Si-N layers on the two sides, one can expect that all p_z orbitals in the original graphene layer are passivated, and the system should become a semiconductor. This picture is confirmed by our result in Fig. 3(c). The resulting semiconducting ML $CSiN$ has valence-band maximum and conduction-band minimum (CBM) located at H and M points, respectively. Here, H is a point on the Γ - M path as indicated in Fig. 3(c). The indirect band gap is about 2.52 eV at the PBE level, and is enlarged to 3.73 eV at the Heyd-Scuseria-Ernzerhof level (see the Supplemental Material Fig. S5 [29]). From the orbital projection, the valence band is highly dominated by the C - p_z and N - p_z orbitals, whereas the conduction band is mostly contributed by Si - $p_{x,y}$ orbitals, which are in line with the real-space par-

tial charge-density analysis (see the Supplemental Material Fig. S6 [29]).

Interestingly, the CBM of ML $CSiN$ exhibits a ternary valley structure, completely different from the binary valley structure in pristine graphene. Consider the electron-doped case. As illustrated in Fig. 5(a), there are three inequivalent valleys for the conduction band, centered at the three M points of the Brillouin zone. The three valleys are connected by the C_{3z} symmetry, which enforces their energy degeneracy. Each electron carrier can be assigned a valley label M_i with $i = 1-3$.

There is a crucial distinction between ML $CSiN$ and the existing valleytronic platforms, such as graphene or 2D transition-metal dichalcogenides [13–15,43]. For the latter, the valleys are connected by the time-reversal symmetry \mathcal{T} . It follows that to generate valley splitting or valley polarization, one must break the \mathcal{T} symmetry, e.g., by using the applied magnetic field [44], circularly polarized light [6], or by nonequilibrium transport [5]. In contrast, for ML $CSiN$, the three valleys are not connected by \mathcal{T} , instead, they are only related by a crystalline symmetry. Therefore, valley splitting and valley polarization in this system can be generated in a *static*

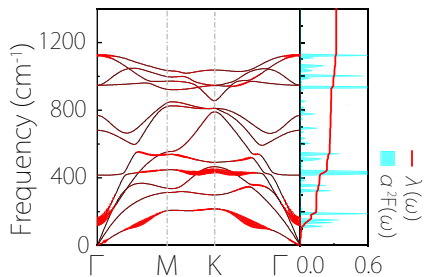


FIG. 4. The weighted EPC λ_{qv} in the phonon spectrum. The right panel shows the Eliashberg function $\alpha^2F(\omega)$ with cumulative EPC constant $\lambda(\omega)$.

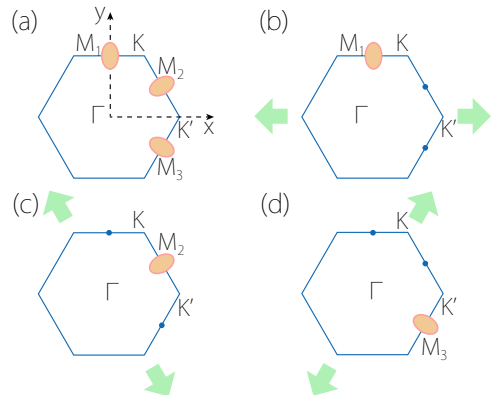


FIG. 5. (a) Schematic figure showing the three M valleys for the electron carriers in ML $CSiN$. These valleys are degenerate in energy due to the C_{3z} symmetry. (b) Under a uniaxial tensile strain along x , M_1 valley shifts down in energy [see Fig. 6(a)]. Under small electron doping, all electron carriers are polarized in the M_1 valley. (c) and (d) illustrate the cases when the strain is applied along the other two zigzag directions, showing that one can control the valley polarization by strain.

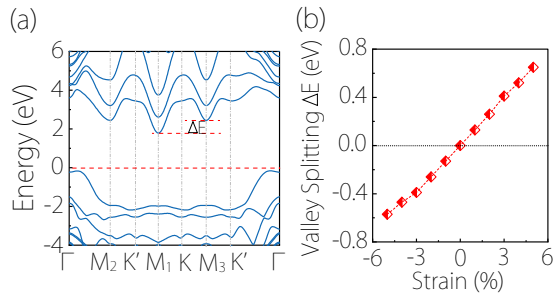


FIG. 6. (a) Band structure for ML CSiN at the 5% tensile strain along the x direction. (b) Valley splitting ΔE as a function of uniaxial strain along x .

way, e.g., by using lattice strains that break the crystalline symmetry. For 2D materials, strain can be readily applied, e.g., by a beam-bending apparatus or by using piezoelectric substrates [45,46].

The above point is nicely demonstrated in our calculation. As shown in Fig. 6(a), by applying a uniaxial strain along the x direction, the C_{3z} symmetry is broken and the valley M_1 exhibits an energy splitting from the other two valleys. Figure 6(b) shows the valley splitting as a function of the applied strain. The valley splitting can be as large as $\Delta E_V = 0.64$ eV at a moderate strain of $\varepsilon = 5\%$. The susceptibility of the valley splitting to the strain can be characterized by the slope of the curve,

$$\chi_V = \left. \frac{d(\Delta E_V)}{d\varepsilon} \right|_{\varepsilon=0} / 100, \quad (1)$$

which is about 130 meV for ML CSiN. At a small doping level, all the electron carriers will be falling into this M_1 valley, creating a large valley polarization of the carriers [see Fig. 5(b)]. Similarly, by choosing the direction for applying strain, one can control the valley label of the carriers as illustrated in Figs. 5(c) and 5(d). As discussed, such a valley control scheme is not possible with the conventional valleytronic platforms.

Furthermore, we show that the valley polarization in ML CSiN features a large transport anisotropy, hence, it can be detected by electric means. Let us first consider the unstrained case without valley splitting. The mobility of electron carriers can be estimated by the following formula [47,48]:

$$\mu_i^{2D} = \frac{e\hbar^3 C_i^{2D}}{k_B T m_d^* m_i^* (D_i)^2}, \quad (2)$$

where i labels an in-plane direction, $C_i^{2D} = (1/S_0)(\partial^2 E_S / \partial \varepsilon_i^2)$ is the 2D elastic constant, E_S and S_0 are the energy and area of the system, ε_i is the strain in the i direction, T is the room temperature (300 K), m_i^* is the effective mass along i , $m_d^* = (m_x^* m_y^*)^{1/2}$ is an average effective mass, and $D_i = \partial \Delta / \partial \varepsilon_i$ is the deformation potential constant with Δ as the shift of band edge under strain. Note that without strain, there are three degenerate valleys, so the calculation has to average over the three valleys. Calculated data were given in Table S4 in the Supplemental Material [29]. The obtained electron mobility for unstrained ML CSiN is $\mu_x \approx 940$ cm² V⁻¹ S⁻¹, and $\mu_y \approx 2391$ cm² V⁻¹ S⁻¹. Here, x and y directions are

indicated in Fig. 1, which are the zigzag and armchair directions, respectively. These values are larger or comparable to those in MoS₂ (~ 200 cm² V⁻¹ s⁻¹) [49] and phosphorene (~ 1000 cm² V⁻¹ s⁻¹) [50].

Now we consider a 5% uniaxial strain applied in the x direction. As shown in Fig. 6(a), the CBM lies in only one valley, the M_1 valley, and at low doping, the electrons are fully valley polarized in this valley. Importantly, the individual valley is highly anisotropic (the little co-group at M point is C_s), which can be readily seen from the effective masses. For the M_1 valley, we find $m_x^* = 0.26m_e$ and $m_y^* = 0.81m_e$. By using the formula (2), we obtain that when the carriers are valley polarized in the M_1 valley, the mobility becomes $\mu_x = 1388$ cm² V⁻¹ S⁻¹ and $\mu_y = 270$ cm² V⁻¹ S⁻¹. One observes that the ratio μ_x/μ_y changes by about ten times from $\sim 1/2$ at unstrained case to ~ 5 at 5% strain. This can be readily detected as an anisotropy in the conductivity $\sigma_x/\sigma_y \approx \mu_x/\mu_y$.

Therefore, in ML CSiN, we can use moderate strain to induce highly anisotropic electron transport. For valleytronic applications, the system offers a novel ternary valley structure. The valley splitting and polarization can be readily controlled by strain in a static manner. One can encode information into this valley polarization and transport information by the valley-polarized charge current. And the information can be read out in a fully electric way by measuring the anisotropy in conductivity/resistivity. Furthermore, the ternary valley degree of freedom may serve as a qutrit, which, under suitable circumstances, could be more stable against decoherence than qubits [51]. Nevertheless, how to achieve coherent manipulation of such qutrits in the material system still needs to be explored.

E. Excitonic effect in ML CSiN

We have shown that ML CSiN is a good semiconductor. Typically, 2D semiconductors have strong excitonic effects due to the reduced screening of Coulomb interactions [37,52]. To capture this effect, we adopt the GW approximation based on the quantum many-body perturbation theory [53] to explore the optical properties. The frequency-dependent 2D polarizability of the material can be obtained from [54]

$$\alpha_{2D}(\omega) = - \lim_{\mathbf{q} \rightarrow 0} \frac{\chi(\mathbf{q}, \omega)}{\mathbf{q}^2}, \quad (3)$$

where \mathbf{q} is the in-plane wave vector and χ is the polarizability function. The imaginary part of $\alpha_{2D}(\omega)$ reflects the optical absorption property of the material. For ML CSiN, the results are plotted in Fig. 7(a). Here, we have taken two approaches: one is GW plus the RPA ($GW + RPA$) [without electron-hole (e-h) interactions] and the other is GW plus the BSE ($GW + BSE$) (with e-h interactions). Their difference can manifest the exciton contribution.

One observes that when e-h interactions are taken into consideration, a sharp exciton absorption peak emerges at about 4.91 eV (the optical gap). According to the spectral edge from $GW + RPA$ calculation, the G_0W_0 gap is about 6.0 eV. Then, the exciton binding energy is estimated to be about 1.09 eV and is mainly associated with direct transitions at the Γ point. This binding energy is larger than that in MoS₂ (0.80 eV)

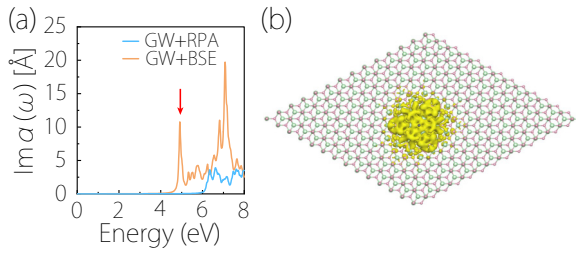


FIG. 7. (a) Imaginary part of the transverse dielectric function of ML CSiN, calculated at the level of $G_0W_0 + \text{RPA}$ and $G_0W_0 + \text{BSE}$. (b) Spatial distribution of the first bright exciton [marked by the arrow in (a)]. Here, we use a $13 \times 13 \times 1$ supercell. The hole position is marked by the black spot at the center. The isosurface value is set to be $0.03 e/\text{\AA}^3$.

[55], ML Janus-MoSSe (0.95 eV) [56], and GeSe (0.40 eV) [57] due to its larger band gap with weaker screening. The spatial extent of the exciton state can be studied by plotting the magnitude of the exciton wave function given by

$$|\psi(\mathbf{r}_e, \mathbf{r}_h)| = \sum_{c\nu\mathbf{k}} A_{c\nu\mathbf{k}}^S \psi_{c\nu\mathbf{k}}(\mathbf{r}_e) \psi_{c\nu\mathbf{k}}(\mathbf{r}_h), \quad (4)$$

where $A_{c\nu\mathbf{k}}^S$ is the e-h amplitude, and \mathbf{r}_e and \mathbf{r}_h denote the electron and hole coordinates, respectively. In Fig. 7(d), we plot the spatial distribution for the first exciton peak. One clearly sees that the exciton is tightly bonded with a narrow radius $\sim 5.83 \text{ \AA}$, consisting with its strong binding energy. From Fig. 7(a), we can conclude that ML CSiN exhibits strong excitonic effect, which greatly enhances its optical absorption in the ultraviolet range.

IV. DISCUSSION AND CONCLUSION

Graphene is chemically unsaturated. Carbon atoms can form an extra covalent bond during chemical functionalization, which converts the hybridization of carbon atoms from sp^2 to sp^3 . In fact, hydrogenated [9,58,59], fluorinated [10,60,61], and oxidized graphene [62,63] have all been synthesized. Recently, centimeter-scale monolayers of MoSi_2N_4 were synthesized via chemical vapor deposition growth, which can be viewed as MoN_2 monolayers passivated

by Si-N layers on the two sides. The materials proposed here may be synthesized via a similar approach by introducing the Si element to passivate the surface dangling bonds of freestanding graphene in the NH_3 gas environment [11]. Once achieved, forming tunnel barriers or contacts to ML CSiN should not be a problem since the material is a good semiconductor, and the outer Si-N layers are also quite inert.

In conclusion, we propose two graphene-based 2D materials, the ML C_2SiN and CSiN, motivated by the recent experimental progress on 2D structures passivated with Si-N layers. We find that C_2SiN is a metal and exhibits superconductivity unavailable in pristine graphene. The ML CSiN has excellent stability and mechanical property. It is an indirect gap semiconductor with band gap $>3 \text{ eV}$, and its electron mobility can reach $\sim 2000 \text{ cm}^2 \text{ V}^{-1} \text{ S}^{-1}$. Importantly, ML CSiN has a ternary valley structure for electron carriers. In contrast to existing valleytronic platforms, the valleys in ML CSiN are connected by a crystalline symmetry instead of the time-reversal symmetry. This enables a static control of valley polarization in ML CSiN, e.g., by uniaxial strain. We show that the valley polarization can be readily detected via purely electric measurement as an anisotropy in the conductivity. Finally, we show strong excitonic effects in ML CSiN with large exciton binding energy $\sim 1 \text{ eV}$ and strong absorption peak in the ultraviolet range. Our paper reveals a novel type of 2D valleytronic platform with new valley control and detection mechanisms. Based on their excellent properties, the two new materials could also find useful applications in mechanical, electronic, and optical devices.

ACKNOWLEDGMENTS

We thank D. L. Deng for valuable discussions. This work was supported by the Startup funds of Outstanding Talents of UESTC (Grant No. A1098531023601205), National Youth Talents Plan of China (Grant No. G05QNQR049), the Open-Foundation of Key Laboratory of Laser Device Technology, China North Industries Group Corporation Limited (Grant No. KLLDT202106), and Singapore MOE AcRF Tier 2 (Grant No. MOE-T2EP50220-0011). B.-T.W. acknowledges financial support from the Natural Science Foundation of China (Grants No. 11675195 and No. 12074381) and Guangdong Basic and Applied Basic Research Foundation (Grant No. 2021A1515110587).

[1] K. S. Novoselov, A. K. Geim, S. V. Morozov, D. Jiang, Y. Zhang, S. V. Dubonos, I. V. Grigorieva, and A. A. Firsov, *Science* **306**, 666 (2004).
 [2] A. H. Castro Neto, F. Guinea, N. M. R. Peres, K. S. Novoselov, and A. K. Geim, *Rev. Mod. Phys.* **81**, 109 (2009).
 [3] J. R. Schaibley, H. Yu, G. Clark, P. Rivera, J. S. Ross, K. L. Seyler, W. Yao, and X. Xu, *Nat. Rev. Mater.* **1**, 16055 (2016).
 [4] A. Rycerz, J. Tworzydło, and C. Beenakker, *Nat. Phys.* **3**, 172 (2007).
 [5] D. Xiao, W. Yao, and Q. Niu, *Phys. Rev. Lett.* **99**, 236809 (2007).
 [6] W. Yao, D. Xiao, and Q. Niu, *Phys. Rev. B* **77**, 235406 (2008).

[7] H. Min, J. E. Hill, N. A. Sinitsyn, B. R. Sahu, L. Kleinman, and A. H. MacDonald, *Phys. Rev. B* **74**, 165310 (2006).
 [8] J. C. Boettger and S. B. Trickey, *Phys. Rev. B* **75**, 121402(R) (2007).
 [9] D. C. Elias, R. R. Nair, T. Mohiuddin, S. Morozov, P. Blake, M. Halsall, A. C. Ferrari, D. Boukhvalov, M. Katsnelson, A. Geim *et al.*, *Science* **323**, 610 (2009).
 [10] K.-J. Jeon, Z. Lee, E. Pollak, L. Moreschini, A. Bostwick, C.-M. Park, R. Mendelsberg, V. Radmilovic, R. Kostecki, T. J. Richardson *et al.*, *ACS Nano* **5**, 1042 (2011).
 [11] Y.-L. Hong, Z. Liu, L. Wang, T. Zhou, W. Ma, C. Xu, S. Feng, L. Chen, M.-L. Chen, D.-M. Sun *et al.*, *Science* **369**, 670 (2020).

- [12] J. Liu, Z. Liu, T. Song, and X. Cui, *J. Mater. Chem. C* **5**, 727 (2017).
- [13] S. Li, Q. Wang, C. Zhang, P. Guo, and S. A. Yang, *Phys. Rev. B* **104**, 085149 (2021).
- [14] S. Li, W. Wu, X. Feng, S. Guan, W. Feng, Y. Yao, and S. A. Yang, *Phys. Rev. B* **102**, 235435 (2020).
- [15] Q. Wang, L. Cao, S.-J. Liang, W. Wu, G. Wang, C. H. Lee, W. L. Ong, H. Y. Yang, L. K. Ang, S. A. Yang *et al.*, *npj 2D Mater Appl* **5**, 71 (2021).
- [16] P. E. Blöchl, *Phys. Rev. B* **50**, 17953 (1994).
- [17] P. E. Blöchl, O. Jepsen, and O. K. Andersen, *Phys. Rev. B* **49**, 16223 (1994).
- [18] G. Kresse and J. Furthmüller, *Phys. Rev. B* **54**, 11169 (1996).
- [19] G. Kresse and D. Joubert, *Phys. Rev. B* **59**, 1758 (1999).
- [20] Jiří Klimeš, D. R. Bowler, and A. Michaelides, *Phys. Rev. B* **83**, 195131 (2011).
- [21] A. Togo and I. Tanaka, *Scr. Mater.* **108**, 1 (2015).
- [22] S. Nosé, *J. Chem. Phys.* **81**, 511 (1984).
- [23] V. Wang, N. Xu, J.-C. Liu, G. Tang, and W.-T. Geng, *Comput. Phys. Commun.* **267**, 108033 (2021).
- [24] P. Giannozzi, S. Baroni, N. Bonini, M. Calandra, R. Car, C. Cavazzoni, D. Ceresoli, G. L. Chiarotti, M. Cococcioni, I. Dabo *et al.*, *J. Phys.: Condens. Matter* **21**, 395502 (2009).
- [25] P. Giannozzi, O. Andreussi, T. Brumme, O. Bunau, M. B. Nardelli, M. Calandra, R. Car, C. Cavazzoni, D. Ceresoli, M. Cococcioni *et al.*, *J. Phys.: Condens. Matter* **29**, 465901 (2017).
- [26] J. Bardeen, L. N. Cooper, and J. R. Schrieffer, *Phys. Rev.* **108**, 1175 (1957).
- [27] X. Zhang, Y. Zhou, B. Cui, M. Zhao, and F. Liu, *Nano Lett.* **17**, 6166 (2017).
- [28] F. Giustino, *Rev. Mod. Phys.* **89**, 015003 (2017).
- [29] See Supplemental Material at <http://link.aps.org/supplemental/10.1103/PhysRevB.107.085413> for detailed methods for calculating superconductivity, ELF plots, AIMD simulations for C₂SiN monolayer, variations of stress and strain energy with respect to strains, variation of T_c under external strains, band structures of CSiN monolayer from hybrid functional methods, partial charge density distributions, atomic positions, mechanical properties, and carrier mobility.
- [30] P. B. Allen and R. Dynes, *Phys. Rev. B* **12**, 905 (1975).
- [31] A. Marini, C. Hogan, M. Grüning, and D. Varsano, *Comput. Phys. Commun.* **180**, 1392 (2009).
- [32] M. Gao, Q.-Z. Li, X.-W. Yan, and J. Wang, *Phys. Rev. B* **95**, 024505 (2017).
- [33] B. Song, Y. Zhou, H.-M. Yang, J.-H. Liao, L.-M. Yang, X.-B. Yang, and E. Ganz, *J. Am. Chem. Soc.* **141**, 3630 (2019).
- [34] L. Yan, P.-F. Liu, H. Li, Y. Tang, J. He, X. Huang, B.-T. Wang, and L. Zhou, *npj Comput. Mater.* **6**, 94 (2020).
- [35] J. Carrete, W. Li, L. Lindsay, D. A. Broido, L. J. Gallego, and N. Mingo, *Mater. Res. Lett.* **4**, 204 (2016).
- [36] F. Mouhat and F.-X. Coudert, *Phys. Rev. B* **90**, 224104 (2014).
- [37] L. Zhou, Z. Zhuo, L. Kou, A. Du, and S. Tretiak, *Nano Lett.* **17**, 4466 (2017).
- [38] M. J. Varjovi, M. Yagmurcukardes, F. M. Peeters, and E. Durgun, *Phys. Rev. B* **103**, 195438 (2021).
- [39] C. Lee, X. Wei, J. W. Kysar, and J. Hone, *Science* **321**, 385 (2008).
- [40] M. Topsakal and S. Ciraci, *Phys. Rev. B* **81**, 024107 (2010).
- [41] Q. Peng and S. De, *Phys. Chem. Chem. Phys.* **15**, 19427 (2013).
- [42] Y. Cao, V. Fatemi, S. Fang, K. Watanabe, T. Taniguchi, E. Kaxiras, and P. Jarillo-Herrero, *Nature (London)* **556**, 43 (2018).
- [43] C. Si, Z. Liu, W. Duan, and F. Liu, *Phys. Rev. Lett.* **111**, 196802 (2013).
- [44] T. Cai, S. A. Yang, X. Li, F. Zhang, J. Shi, W. Yao, and Q. Niu, *Phys. Rev. B* **88**, 115140 (2013).
- [45] K. S. Kim, Y. Zhao, H. Jang, S. Y. Lee, J. M. Kim, K. S. Kim, J.-H. Ahn, P. Kim, J.-Y. Choi, and B. H. Hong, *Nature (London)* **457**, 706 (2009).
- [46] H. J. Conley, B. Wang, J. I. Ziegler, R. F. Haglund, Jr., S. T. Pantelides, and K. I. Bolotin, *Nano Lett.* **13**, 3626 (2013).
- [47] S. Bruzzone and G. Fiori, *Appl. Phys. Lett.* **99**, 222108 (2011).
- [48] J. Qiao, X. Kong, and Z. Hu, *Nat. Commun.* **5**, 4475 (2014).
- [49] Y. Cai, G. Zhang, and Y.-W. Zhang, *J. Am. Chem. Soc.* **136**, 6269 (2014).
- [50] H. Liu, A. T. Neal, Z. Zhu, Z. Luo, X. Xu, D. Tománek, and P. D. Ye, *ACS Nano* **8**, 4033 (2014).
- [51] A. Melikidze, V. V. Dobrovitski, H. A. De Raedt, M. I. Katsnelson, and B. N. Harmon, *Phys. Rev. B* **70**, 014435 (2004).
- [52] L. Yan, J. Zhu, B.-T. Wang, J. He, H.-Z. Song, W. Chu, S. Tretiak, and L. Zhou, *Nano Lett.* **22**, 5592 (2022).
- [53] L. Hedin, *Phys. Rev.* **139**, A796 (1965).
- [54] F. A. Rasmussen, P. S. Schmidt, K. T. Winther, and K. S. Thygesen, *Phys. Rev. B* **94**, 155406 (2016).
- [55] H. Jin, T. Wang, Z.-R. Gong, C. Long, and Y. Dai, *Nanoscale* **10**, 19310 (2018).
- [56] C. Long, Y. Dai, and H. Jin, *Phys. Rev. B* **104**, 125306 (2021).
- [57] L. C. Gomes, P. E. Trevisanutto, A. Carvalho, A. S. Rodin, and A. H. Castro Neto, *Phys. Rev. B* **94**, 155428 (2016).
- [58] E. J. Duplock, M. Scheffler, and P. J. D. Lindan, *Phys. Rev. Lett.* **92**, 225502 (2004).
- [59] R. Balog, B. Jørgensen, L. Nilsson, M. Andersen, E. Rienks, M. Bianchi, M. Fanetti, E. Lægsgaard, A. Baraldi, S. Lizzit *et al.*, *Nature Mater.* **9**, 315 (2010).
- [60] J. T. Robinson, J. S. Burgess, C. E. Junkermeier, S. C. Badescu, T. L. Reinecke, F. K. Perkins, M. K. Zalalutdniov, J. W. Baldwin, J. C. Culbertson, P. E. Sheehan *et al.*, *Nano Lett.* **10**, 3001 (2010).
- [61] R. Zbořil, F. Karlický, A. B. Bourlinos, T. A. Steriotis, A. K. Stubos, V. Georgakilas, K. Šafářová, D. Jančík, C. Trapalis, and M. Otyepka, *Small* **6**, 2885 (2010).
- [62] D. Pandey, R. Reifengerger, and R. Piner, *Surf. Sci.* **602**, 1607 (2008).
- [63] M. Hossain, J. E. Johns, K. H. Bevan, H. J. Karmel, Y. T. Liang, S. Yoshimoto, K. Mukai, T. Koitaya, J. Yoshinobu, M. Kawai *et al.*, *Nat. Chem.* **4**, 305 (2012).